

Modelling of Microstructure Evolution in Wire-Based Laser Direct Energy Deposition with Ti-6Al-4V

Yousub Lee^{1*}, Srdjan Simunovic¹, Brian Gibson², Paritosh Mhatre², Alex Roschli²

¹ Computational Sciences and Engineering Division, Oak Ridge National Laboratory, Oak Ridge, TN, USA

² Manufacturing Science Division, Oak Ridge National Laboratory, Oak Ridge, TN, USA

*Corresponding author: leey@ornl.gov

Abstract

Over the past years, wire-based direct energy deposition (DED) has been transitioning from rapid prototyping to the production of end-use part and mass production. However, a wide market penetration of the DED has not happened yet. The difficulties for wide-scale market adoption to critical structural components are related to the development cost for process optimization and for manufacturing of high-quality parts. For metallic components, the process conditions (e.g., power, speed, tool path) control the material and mechanical properties/performance of the printed part. The thermal history strongly determines the phase fraction, morphology, growth pattern, size of microstructure, and nature of defects. Thus, in this study, we: 1) developed a thermal simulation using finite element method, 2) experimentally measured thermal histories from a U-shaped part with four tool paths of horizontal, vertical, raster, and contour to calibrate and validate the thermal model, and 3) investigated the effect of thermal history on microstructure evolution and quantified the microstructural variation during the printing process.

1. Introduction

Wire-based direct energy deposition (DED) is one of the promising metal additive manufacturing (AM) technologies. Since DED provides high-deposition rates (up to 5 kg/h), high-material efficiency (up to 100%), and less costly wire/system (stainless steel wire ~\$10/kg) [1], it is known as an ideal additive manufacturing (AM) process for creating large-scale components with moderate complexity. For instance, the manufacturing envelop of this process can be millimeter to meter-scale. Despite its ability to create large components in a cost-effective manner, two primary challenges still hinder a wide-scale market adoption of this technology to critical structural components for aerospace and other industrial applications: 1) large distortion and residual stress, and 2) anisotropy in microstructure and material/mechanical properties. As DED technology transitions from prototyping to the production of end-use part and mass production [2], the challenges should be urgently overcome for tight control of properties and performance.

Over past years, numerous parameter optimization studies in the wire-based DED have reported that there is a strong influence of manufacturing parameters including power, speed, tool path, dwell time, and part geometry on temperature profile during printing and resultant microstructure, and part performance [3-8]. The thermal history, in turn, significantly affects phase fraction, grain morphology, growth pattern, size of microstructure, and nature of defects. It can further influence the final part properties/performance such as yield strength, fatigue, stiffness, and creep life. Therefore, a comprehensive understanding of the correlation between process parameters, microstructure, and

Notice of Copyright. This manuscript has been authored by UT-Battelle, LLC under Contract No. DE-AC05-00OR22725 with the U.S. Department of Energy. The United States Government retains and the publisher, by accepting the article for publication, acknowledges that the United States Government retains a non-exclusive, paid-up, irrevocable, world-wide license to publish or reproduce the published form of this manuscript, or allow others to do so, for United States Government purposes. The Department of Energy will provide public access to these results of federally sponsored research in accordance with the DOE Public Access Plan (<http://energy.gov/downloads/doe-public-access-plan>).

mechanical performance is required to maintain high-quality components. Although physical processes during large-scale AM are analogues to welding [9, 10] or powder bed AM [11-13], the process involves widely varying time and length scale that leads to complex interactions between part geometry, process, and spatial and temporal variation of microstructure. Moreover, those factors are considerably magnified in large-scale AM as the part size becomes larger and complex. Therefore, AM of realistic geometries for large-scale AM still requires exhaustive experimental trial and error optimization.

The most common way to assure final part quality in AM is to characterize microstructure (e.g., size, type, shape, orientation, etc.) using optical microscope, scanning electron microscope, and electron backscattered diffraction [5, 14]. These image analysis methods require laborious polishing/sectioning of samples and numerous images due to limited resolution areas. For instance, α lath thickness in Ti-6Al-4V requires high magnification in length-scale that should resolve a couple of hundreds of μm . Thus, the experimental measurement over the entire part volume is highly laborious and/or not practical in terms of cost and rapid qualification. Numerical modeling can be an effective alternative for the microstructure characterization over the full part volume. Thanks to the recent advancement of computing capability, the key microstructure features have been further understood but characterizing microstructure is still difficult for large-scale DED due to large part size (feet-scale) and long printing time (days or even months), requiring fine time resolution (s) and spatial resolution (mm) for the characterization.

The objective of this research is to develop a prediction capability of thermal history for the large-scale wire-based laser DED process and predict microstructure evolution in various tool paths. Four tool paths of horizontal, vertical, raster, and contour were explored to investigate the influence of tool path on microstructure evolution on U-shaped part. The predicted thermal history is validated with measured thermal data using two statistical methods of Pearson coefficient and mean absolute error (MAE). Finally, the predicted microstructure of Ti-6Al-4V is analyzed in terms of phase fraction and grain size evolution on the U-shaped part. The developed models can be used on typical desktop computers and can provide predictions of thermal history and spatial and temporal phase transformations at multiple locations in the part.

2. Experimental Measurement

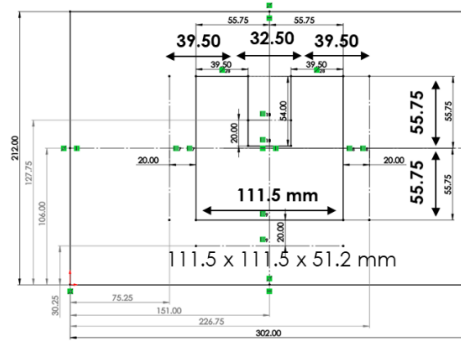
2.1. Printing conditions and tool paths

A prototype U-shaped part was selected for the demonstration of the tool path effect on microstructure evolution. The part was printed with a six-axis KUKA robot system [15]. A fiber laser with power of 8.7 kW and printing speed of 8.0 mm/s were used to form the deposition layers. The U-shaped part contains 32 layers in the build height of 51.2 mm. The printing parameters are summarized in Fig.1(a). The experiments included measurement of the thermal history at selected part locations in Fig. 1(b). A layer height of 1.6 mm and bead width of 12.5 mm were set for four tool paths of horizontal, vertical, raster, and contour as shown in Fig.1(c). The total deposition time is approximately 25,000s, 18,000s, 14,000s, and 10,000s for horizontal, vertical, raster, and contour, respectively. The printed part with contour tool path is shown in Fig. 2.

(a) Printing parameters

Parameter	Value
Laser Power	8.7 kW
Print Speed	8.0 mm/s
Layer height	1.6 mm
Build height	51.2 mm
Bead width	12.5 mm
Hot wire power	370 W
Stepover	9.0 mm

(b) Part dimension and TC locations



(c) Four tool paths

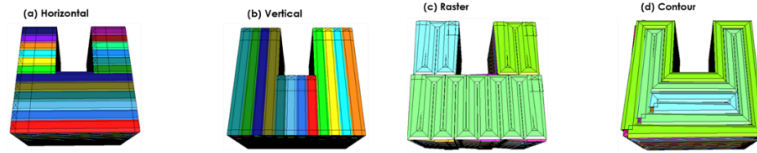


Figure 1. Printing conditions and tool path: (a) printing parameters, (b) part dimension and thermocouple locations, and (c) four tool paths used for the print (horizontal, vertical, raster, and contour).

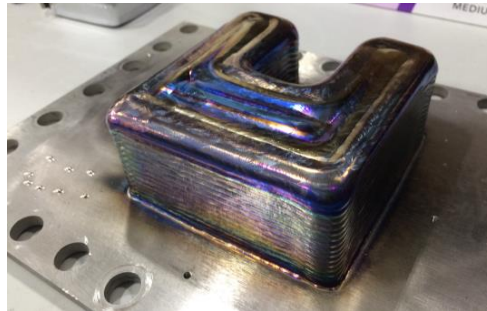


Figure 2. Part printed using L-DED process. The contour tool path was used for this part.

2.2. Temperature history measurement and estimation of the heat transfer coefficient

Under ideal conditions, the titanium build plate and the steel base plate should be in full contact with no gap between them. However, the two contacting surfaces of the solid plates are not perfectly smooth, having a variable gap along their interface. A precise determination of gap conductance requires extensive and complicated experiments. In practical AM, however, the two plates will have shape variations resulting from tolerances in their production process. Therefore, for a practical process simulation, the heat transfer coefficient at the interface should be estimated from thermal measurement and adjusted as the production process changes.

Twelve thermo-couples (TC) were placed to measure temperature variations during deposition. Four TCs marked with red color in Fig. 3(a) were located on the Ti-plate close to the center (TC-16 and TC-22) and side (TC-17 and TC-19) of the U-shaped part. The other eight TCs marked with blue color in Fig.2(a) were positioned at the interface between the Ti plate and the steel plate to estimate the heat transfer through the plates (TC-11, TC-13, TC-14, and TC-15 were on the Ti-plate, and TC-12, TC-18, TC-20, and TC-21 were on the steel-plate). Fig. 3(b) shows the temperature difference between the Ti plate (TC-11) and the steel plate (TC-20). The averaged ΔT in Table 1 is 8.17°C, 4.28°C, and 5.19°C for the left, center, and right region, respectively. The corresponding estimated

heat transfer coefficients are 0.12, 0.23, and 0.19. The ratio between the coefficients when normalized to the middle value are 0.52:1:0.83 which were used for the calibration of the heat transfer model.

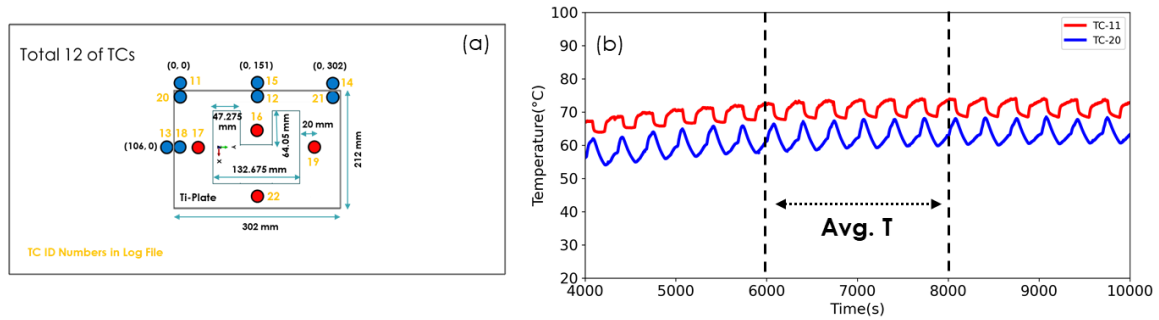


Figure 3. (a) Location of thermo-couples, and (b) temperature difference at between Ti- and steel-plate.

Table 1. Temperature difference and estimated heat transfer coefficient at the left, center, and right region at the interface between the Ti plate and the steel plate

<i>Left: Average TC temperature and heat transfer coefficient (h)</i>				
TC-20	TC-11	ΔT	h	h ratio
63.21°C	71.38°C	8.17	0.12	0.52
<i>Center: Average TC temperature and heat transfer coefficient</i>				
TC-12	TC-15	ΔT	h	h ratio
82.68°C	86.97°C	4.28	0.23	1.00
<i>Right: Average TC temperature and heat transfer coefficient</i>				
TC-21	TC-14	ΔT	h	h ratio
73.36°C	78.55°C	5.19	0.19	0.83

3. Simulation Methodology

Figure 4 shows a solution domain for thermal simulation. The computation domain was created using a mesh generation toolkit CUBIT by Sandia National Laboratory. The characteristic mesh size used in the simulation was 1.6 mm for Ti-wall and Ti-plate, which is identical to a layer thickness of the printed part. An approximately three times coarser mesh size was used for 416 stainless steel-base for computational efficiency. The simulation was performed using the commercial finite element method (FEM) package, ABAQUS 2020 & AM modeler plugin [16]. The thermal simulation provides thermal history at each node over the wall, and the history is extracted and fed into the microstructure simulation as an input. The thermal and microstructure simulation both used 8-node linear isoparametric hexahedral elements, DC3D8. The printing tool path was created using Oak Ridge National Laboratory (ORNL) slicer software translating the standard G-code output to the printing machine input command. The actual laser power and travel path are directly converted from G-code to the modeling input values. This machine-related conversion promises minimal loss of simulation accuracy. The material properties used in this simulation can be found in literature [17].

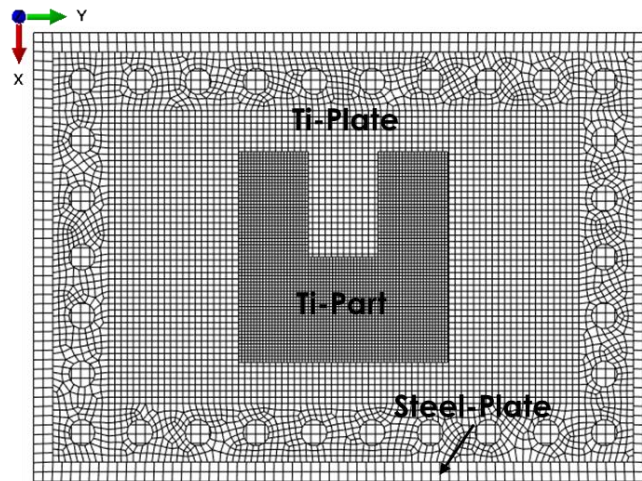


Figure 4. Build geometry of U-shaped part. It consists of Ti-part, Ti-plate, and 416 stainless steel-base.

A phenomenological metallurgical phase transformation model is used to consider solid-state transformation kinetics (i.e., diffusional, non-diffusional, and reversible phase transformation) corresponding to thermal variation based on the Time-Temperature-Transformation (TTT) diagram. The computational work was performed using ABAQUS [16] and a TTT diagram that can be experimentally measured or calculated by commercial Computer Coupling of Phase Diagrams and Thermochemistry (CALPHAD) software such as ThermoCalc [18] and JMatPro [19]. As a result, the model can calculate phase transformation in fraction and type as well as grain growth for the printing and printed part. The volume fraction of a certain phase can be calculated by the time and temperature when the transformation occurs (i.e., TTT diagram). The kinetics of diffusional transformation can be described by the Johnson-Mehl-Avrami model [20, 21]. Diffusionless (=martensitic) transformation is estimated using the empirical Koistinen-Marburger model [21]. Detailed algorithms and equations used for microstructure modeling can be found in prior literature [20-22].

4. Results and Discussion

4.1. Validation of thermal history

A good agreement in thermal characteristics (e.g., thermal history) of the computational model with experiment measurements is necessary for a good accuracy in prediction of distortion and residual stresses. Four tool paths of horizontal, vertical, raster, and contour were explored to investigate the effect of the tool path on temperature profile and plate distortion. Figures 5-6 show a comparison of the predicted temperature profile with the measurements for the full clamped condition. The temperatures were extracted from the model time histories at the same locations of thermocouples TC-16 (top), TC-22 (bottom), TC-17 (left), and TC-19 (right) shown in Fig. 3(a).

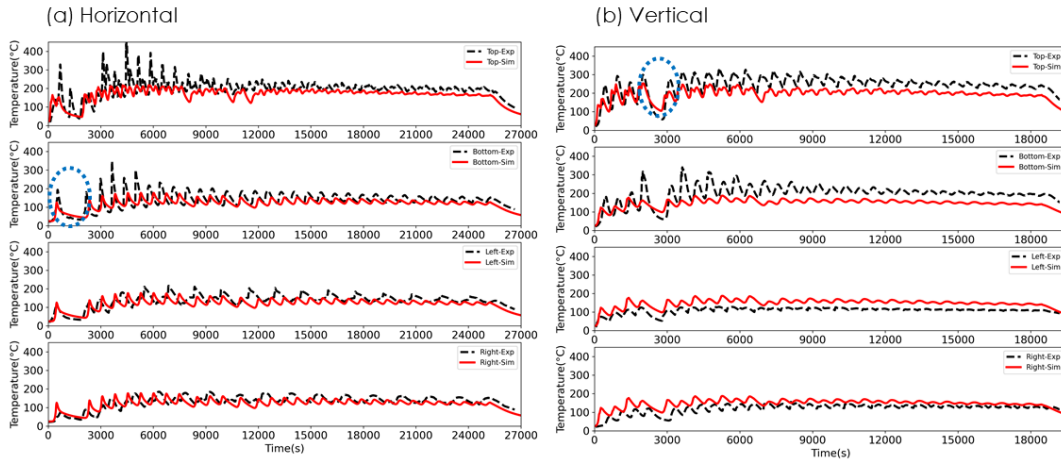


Figure 5. The predicted thermal history (red) at four monitoring locations (black) from (a) horizontal and (b) vertical tool path.

The predicted temperature profiles (denoted by red solid lines) agree reasonably well with the measured profiles (denoted by black dashed lines). Notice that there are abrupt temperature drops indicated with blue dashed circle in horizontal, vertical, and raster tool path. Intermittent pauses were due to adjustments of machine setting. The pauses result in the temperature drops. These pauses cannot be predetermined for simulations before the actual printing commences, so that additional adjustments of simulated process conditions (e.g., adjustment of tool path time and location) are required for better fidelity of the simulation using a build-log file after the completion of printing.

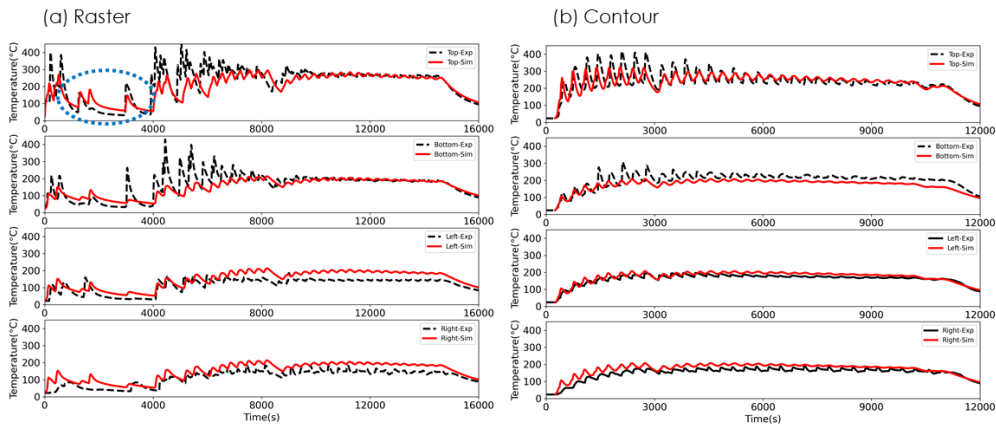


Figure 6. The predicted thermal history at four monitoring locations from (a) raster and (b) contour tool path.

The temperature profiles at each monitoring location are averaged and compared to the predicted average temperatures in Table 2. The relative fractional percentage between the measured and predicted temperature shows 90.9%, 85%, 84.1%, and 81.8% match in overall comparison. In metal additive manufacturing, thermal gyration affects local deformation, phase transformation, and resultant mechanical properties, therefore, the similarity of the thermal profile shape should also be assessed.

Table 2. Comparison of averaged temperatures between measured and predicted at top, bottom, left, and right region in the part shown in Fig.3(a).

Contour						Raster					
Avg. Temp	T	B	L	R	Overall	Avg. Temp	T	B	L	R	Overall
Measured	241.5	203.6	164.1	153.4	90.9%	Measured	148.7	115.0	85.2	88.9	85.0%
Predicted	221.4	164.4	150.3	152.7		Predicted	160.4	121.9	114.1	113.3	
Relative Fraction	0.92	0.81	0.92	1.00		Relative Fraction	0.93	0.94	0.75	0.78	
Horizontal						Vertical					
Avg. Temp	T	B	L	R	Overall	Avg. Temp	T	B	L	R	Overall
Measured	197.7	139.0	137.6	130.8	84.1%	Measured	241.6	198.4	109.7	120.7	81.8%
Predicted	163.1	117.4	114.4	113.0		Predicted	186.4	141.2	130.4	127.4	
Relative Fraction	0.83	0.84	0.83	0.86		Relative Fraction	0.77	0.71	0.84	0.95	

For the detailed comparison of the predicted to measured temperature profile shape, two statistical constants, the Pearson coefficient and MAE were adopted. The two methods compare similarity in shape of the temperature curve and difference in the magnitude of temperature, respectively. The Pearson coefficient shows a mathematical correlation between two continuous variables. The values of ± 1 indicates a perfect linear relationship, and a value of 0 indicates no correlation between the variables. MAE is the average sum of the absolute difference of two variables, $MAE = \sum_{i=1}^n |a_i - b_i|/n$ that indicates a difference in magnitude.

Figure 7 shows the Pearson correlation coefficient and MAE for the four tool paths. On average, the calculated Pearson coefficient is 0.71 for the horizontal path, and 0.92 for the contour path. The values indicate that the shape of the temperature history has strong correlation between the predicted and measured values. Furthermore, the average values of MAE are $\sim 20^\circ\text{C}$ for the contour path and $\sim 37^\circ\text{C}$ for the vertical path. Again, the statistical analysis shows that better prediction accuracy was obtained for the contour and raster tool paths than for the horizontal and vertical tool paths. The variations may be attributed to the differences of the radiation heating towards TCs resulting from different tool paths and heating/cooling intervals.

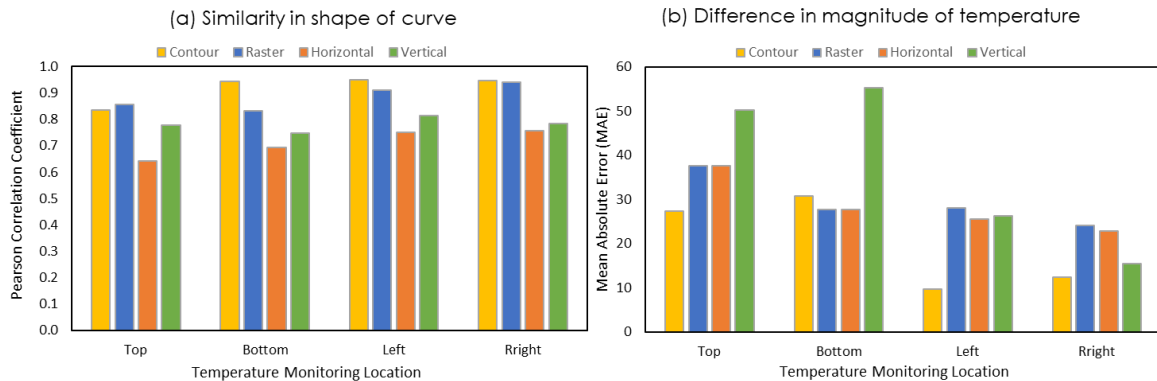


Figure 7. Quantification of (a) similarity and (b) difference between the prediction and measured temperature history.

4.2. Prediction of phase fraction and grain size

A complex thermal cycle brings about spatial and temporal variations in microstructure and the resultant mechanical properties. The microstructural variations are strongly correlated with the process parameters, tool path, and part geometry, which can be used in an optimization scheme including post-heat treatment. Generally, microstructure control in Ti-6Al-4V involves phase fraction and size of α and β . The α phase provides strength and β phase improves ductility of the alloy.

Figure 8 shows a geometric schematic for five monitoring locations in the U-part. The thermal histories were obtained from the simulations for marked locations at 10th, 20th, and 30th layers.

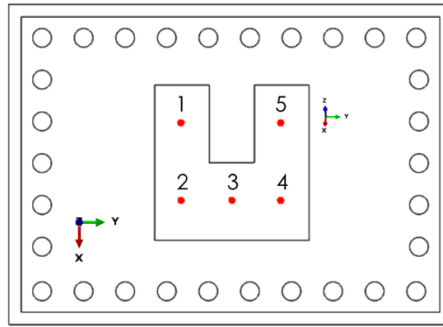


Figure 8. Geometric schematic for five thermal profile monitoring locations.

Figure 9 shows the transient microstructure evolution during deposition on the 10th layer at the location of 1 in Fig. 8. The α and β phase fraction inversely fluctuate with corresponding temperatures. The predicted α and β phase fraction remains almost constant at 92% and 8% after completion of melting and cooling. However, there is observable variations in the α phase fraction and β grain size found at the end of melting.

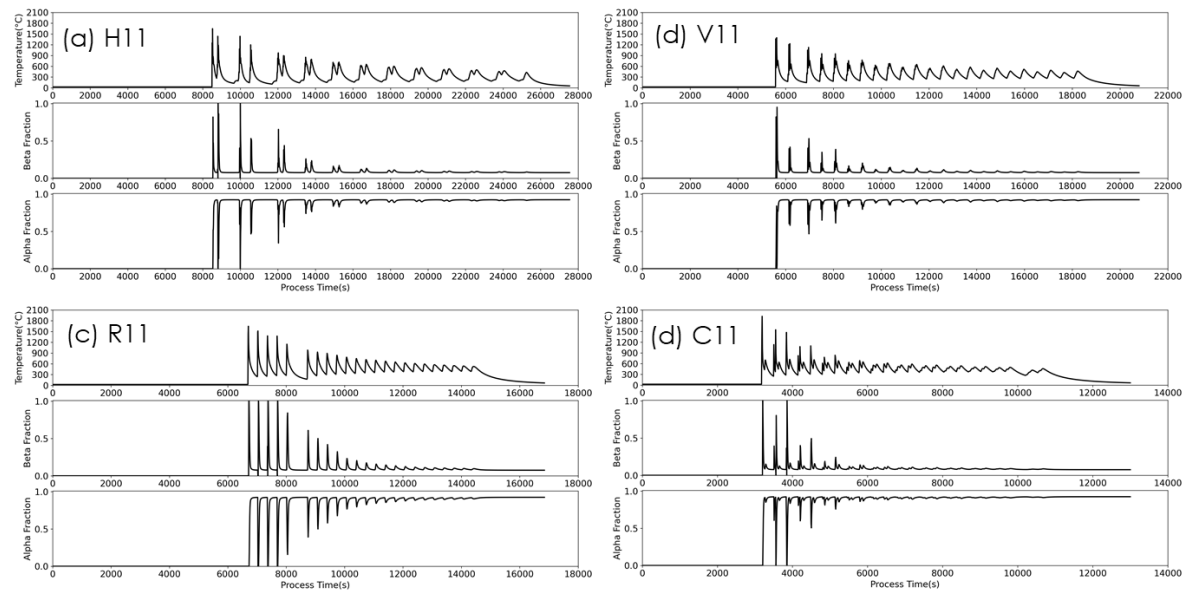


Figure 9. Transient variation of microstructure during deposition on the 10th layer at the location of 1 with (a) horizontal, (b) vertical, (c) raster, and (d) contour tool path.

The variation of α -fraction and β grain size is summarized in Table 3, and 4. The tool paths are categorized into discrete (horizontal and vertical) and continuous (raster and contour) based on the characteristic feature of the melting pattern. In Table 3, the higher α -fraction is observed in the discrete tool path patterns than in the continuous. Also, the lower region of 11 and 13 at the 10th layer shows a slightly higher α -fraction by approximately 0.1%~1% than the upper region of 31 and 33 at the 30th layer.

Table 3. Variation of α -fraction at different tool paths of horizontal, vertical, contour, and raster

		α -Fraction (End of Melting)						
Discrete	H	H11	H13	H21	H23	H31	H33	Avg
		91.86%	73.23%	91.92%	91.26%	91.98%	91.55%	88.63%
	V	V11	V13	V21	V23	V31	V33	Avg
		92.03%	91.78%	91.94%	91.50%	91.76%	90.66%	91.61%
Continuous	C	C11	C13	C21	C23	C31	C33	Avg
		91.37%	81.56%	91.34%	87.67%	91.27%	85.72%	88.16%
	R	R11	R13	R21	R23	R31	R33	Avg
		90.95%	88.38%	89.78%	82.89%	89.32%	69.38%	85.12%

Since β grain size influences the tensile strength of Ti-6Al-4V, controlling of β grain growth and size around a couple of hundred μm is a practical way to balance the tensile, fatigue, and creep properties. The predicted β average grain size is in the range from 170 μm to 273 μm in Table 4. The size varies with the type of tool path. Again, the discrete pattern produces a larger β grain size than the continuous pattern. The corner of region 2 forms larger grain size than that at regions 1 and 3. Notice that a larger grain size is predicted for the longer melting distance (H31 and V11) than the shorter melting distance (H11 and V31). For instance, H31 travels through 2 and 3 to 4 in Fig. 8 whereas H11 melts only 1. V11 moves through 1 to 2 in Fig. 8 while V31 melts 3 only. It indicates that the grain size can be controlled by tool path selection.

Table 4. Variation of β grain size at different tool paths of horizontal, vertical, contour, and raster

		β Grain Size (μm)						
Discrete	H	H11	H13	H21	H23	H31	H33	Avg
		149.8	145.0	379.5	298.4	284.3	250.9	251.3
	V	V11	V13	V21	V23	V31	V33	Avg
		248.7	395.6	346.4	269.5	83.4	296.4	273.3
Continuous	C	C11	C13	C21	C23	C31	C33	Avg
		90.3	38.5	349.1	294.6	219.7	28.1	170.1
	R	R11	R13	R21	R23	R31	R33	Avg
		180.9	235.2	176.7	289.1	205.5	102.6	198.3

5. Concluding Remarks

The prediction capability of thermal history was successfully demonstrated for the large-scale AM parts manufactured using four different tool paths. The thermal model was used to develop a prototype workflow for a coupled thermal and microstructural simulation, and a method for deriving resulting mechanical properties. The following key findings and conclusions can be made from this study:

1. The developed thermal simulation shows the capability of predicting temperature history and changes by tool paths. The simulated temperature profile agrees well with the measured values in both qualitative and quantitative methods.
2. The microstructure evolution is transient and interactive to the variations of thermal cycles during deposition. The different tool paths lead to variations in α fraction and β grain size. Higher α -fractions were found in discrete paths than in continuous paths. Also, the lower region shows a slightly higher α -fraction by 0.1% to 1%.
3. The predicted β grain size is about 170 μm to 273 μm . Large β grain size was observed in discrete (262 μm) than in continuous (184 μm). Larger grain size is observed in the longer melting distances (i.e., H31 and V11) than shorter distances (i.e., H11 and V21).
4. The findings above indicate that the phase fraction and grain size can be controlled by selection of the appropriate tool path.

The predicted thermal histories and microstructure information can be employed to create a full linkage of process-microstructure-property-performance. The microstructure of Ti-6Al-4V can be digitized such as α fraction, α lath thickness, β fraction, and β grain size. Then, it can be used as a statistical input for synthetic microstructure generation toolkit (e.g., Dream3D) that creates a representative 3D synthetic microstructure. Eventually, the synthetic microstructure can be used as an input for crystal plasticity code, DAMASK [23], PRISM [24], or ExaConstit [25].

6. Acknowledgement

The research was sponsored by the US Department of Energy, Office of Energy Efficiency and Renewable Energy, Advanced Manufacturing Office under contract DE-AC05-00OR22725 with UT-Battelle, LLC. This work is also supported in part by Cooperative Research and Development Agreement with GKN Aerospace, under contract No. NFE-15-05725. The authors would like to acknowledge the contribution of the extend ORNL and GKN Aerospace teams, particularly those of Dr. Joshua Vaughan, Aaron Thornton, W. Chad Henry, and Christopher Allison.

7. References

- [1] A. Ramalho, T.G. Santos, B. Bevans, Z. Smoqi, P. Rao, J.P. Oliveira, Effect of contaminations on the acoustic emissions during wire and arc additive manufacturing of 316L stainless steel, *Additive Manufacturing* 51 (2022) 102585.
- [2] D.-G. Ahn, Directed Energy Deposition (DED) Process: State of the Art, *International Journal of Precision Engineering and Manufacturing-Green Technology* 8(2) (2021) 703-742.
- [3] B.T. Gibson, B.S. Richardson, T.W. Sundermann, L.J. Love, Beyond the Toolpath: Site-Specific Melt Pool Size Control Enables Printing of Extra-Toolpath Geometry in Laser Wire-Based Directed Energy Deposition, *Applied Sciences* 9(20) (2019) 4355.
- [4] X. Hu, A. Nycz, Y. Lee, B. Shassere, S. Simunovic, M. Noakes, Y. Ren, X. Sun, Towards an integrated experimental and computational framework for large-scale metal additive manufacturing, *Materials Science and Engineering: A* 761 (2019) 138057.

- [5] M. Shao, S. Vijayan, P. Nandwana, J.R. Jinschek, The effect of beam scan strategies on microstructural variations in Ti-6Al-4V fabricated by electron beam powder bed fusion, *Materials & Design* 196 (2020) 109165.
- [6] J. Wang, X. Lin, J. Li, Y. Hu, Y. Zhou, C. Wang, Q. Li, W. Huang, Effects of deposition strategies on macro/microstructure and mechanical properties of wire and arc additive manufactured Ti6Al4V, *Materials Science and Engineering: A* 754 (2019) 735-749.
- [7] A. Nycz, Y. Lee, M. Noakes, D. Ankit, C. Masuo, S. Simunovic, J. Bunn, L. Love, V. Oancea, A. Payzant, C.M. Fancher, Effective residual stress prediction validated with neutron diffraction method for metal large-scale additive manufacturing, *Materials & Design* 205 (2021) 109751.
- [8] A.N.M. Tanvir, M.R.U. Ahsan, G. Seo, J.-d. Kim, C. Ji, B. Bates, Y. Lee, D.B. Kim, Heat treatment effects on Inconel 625 components fabricated by wire + arc additively manufacturing (WAAM)—part 2: mechanical properties, *The International Journal of Advanced Manufacturing Technology* 110(7) (2020) 1709-1721.
- [9] S. Kou, *Welding metallurgy*, New Jersey, USA 431(446) (2003) 223-225.
- [10] J.C. Lippold, S.D. Kiser, J.N. DuPont, *Welding metallurgy and weldability of nickel-base alloys*, John Wiley & Sons 2011.
- [11] L.N. Carter, C. Martin, P.J. Withers, M.M. Attallah, The influence of the laser scan strategy on grain structure and cracking behaviour in SLM powder-bed fabricated nickel superalloy, *Journal of Alloys and Compounds* 615 (2014) 338-347.
- [12] E. Chauvet, P. Kontis, E.A. Jägle, B. Gault, D. Raabe, C. Tassin, J.-J. Blandin, R. Dendievel, B. Vayre, S. Abed, Hot cracking mechanism affecting a non-weldable Ni-based superalloy produced by selective electron Beam Melting, *Acta Materialia* 142 (2018) 82-94.
- [13] Y. Lee, M.M. Kirka, S. Kim, N. Sridharan, A. Okello, R.R. Dehoff, S.S. Babu, Asymmetric cracking in Mar-M247 alloy builds during electron beam powder bed fusion additive manufacturing, *Metallurgical and Materials Transactions A* 49(10) (2018) 5065-5079.
- [14] M. Neikter, P. Åkerfeldt, R. Pederson, M.-L. Antti, Microstructure characterisation of Ti-6Al-4V from different additive manufacturing processes, *IOP conference series: materials science and engineering*, IOP Publishing, 2017, p. 012007.
- [15] KUKA robot systems, <https://www.kuka.com/en-us/products/robotics-systems>.
- [16] ABAQUS, *Analysis User's Manual*; Dassault Systèmes Simulia Corp: Providence, RI, USA, 2017.
- [17] Y. Lee, Y. Bandari, P. Nandwana, B.T. Gibson, B. Richardson, S. Simunovic, Effect of interlayer cooling time, constraint and tool path strategy on deformation of large components made by laser metal deposition with wire, *Applied Sciences* 9(23) (2019) 5115.
- [18] ThermoCalc., <http://www.thermocalc.com/>.
- [19] N. Saunders, U. Guo, X. Li, A. Miodownik, J.-P. Schillé, Using JMatPro to model materials properties and behavior, *JOM* 55(12) (2003) 60-65.
- [20] A. Crespo, Modelling of heat transfer and phase transformations in the rapid manufacturing of titanium components, *InTech* 2011.
- [21] Q. Zhang, J. Xie, Z. Gao, T. London, D. Griffiths, V. Oancea, A metallurgical phase transformation framework applied to SLM additive manufacturing processes, *Materials & Design* 166 (2019) 107618.
- [22] C.C. Murgau, R. Pederson, L.-E. Lindgren, A model for Ti-6Al-4V microstructure evolution for arbitrary temperature changes, *Modelling and Simulation in Materials Science and Engineering* 20(5) (2012) 055006.
- [23] F. Roters, M. Diehl, P. Shanthraj, P. Eisenlohr, C. Reuber, S.L. Wong, T. Maiti, A. Ebrahimi, T. Hochrainer, H.-O. Fabritius, *DAMASK—The Düsseldorf Advanced Material*

Simulation Kit for modeling multi-physics crystal plasticity, thermal, and damage phenomena from the single crystal up to the component scale, Computational Materials Science 158 (2019) 420-478.

[24] M. Yaghoobi, S. Ganesan, S. Sundar, A. Lakshmanan, S. Rudraraju, J.E. Allison, V. Sundararaghavan, PRISMS-Plasticity: An open-source crystal plasticity finite element software, Computational Materials Science 169 (2019) 109078.

[25] R.A. Carson, S.R. Wopschall, J.A. Bramwell, ExaConstit, Lawrence Livermore National Lab.(LLNL), Livermore, CA (United States), 2019.